In-Situ Simultaneous Synchrotron Small- and Wide-Angle X-ray Scattering Measurement of Poly(vinylidene fluoride) Fibers under Deformation

Jing Wu and Jerold M. Schultz*

Department of Chemical Engineering, University of Delaware, Newark, Delaware 19716

Fengji Yeh, Benjamin S. Hsiao, and Benjamin Chu

Department of Chemistry, State University of New York at Stony Brook, Stony Brook, New York 11794

Received June 7, 1999; Revised Manuscript Received October 7, 1999

ABSTRACT: Poly(vinylidene fluoride) (PVDF) fibers spun at different take-up speeds (10.6−61.0 m/min) were subjected to stretch−hold deformation at room temperature and in-situ simultaneous synchrotron small- and wide-angle X-ray scattering measurements. Crystal transformation from α to β form and morphological changes in lamellar and fibrillar structures were analyzed in detail. All fibers were found to yield at an early stage of deformation, resulting in alternating necked and unnecked regions along the fiber. From the two-dimensional (2-D) wide-angle X-ray diffraction (WAXD) patterns, mixed α and β (minor fraction) forms were found to coexist in the undrawn fibers. Deformation assisted in the conversion from the α-form into the β-form. In necked regions, more α to β transformation took place than in unnecked regions. The overall crystallinity index and unit cell parameters of the α form did not change significantly prior to necking. From the 2-D small-angle X-ray scattering (SAXS) patterns, two kinds of equatorial streaks were observed. The first kind originated from fiber of high take-up speed (61.0 m/min) under zero or small strain, and the second kind came from highly deformed fibers (all take-up speeds) in both necked and unnecked regions. These two kinds of equatorial streaks were attributed to the formation of microfibrils and microvoids, respectively. The dimensions of the lengths of microfibrils and microvoids were estimated by Ruland's method. Meridianal scattering maxima from a lamellar morphology were observed in the SAXS patterns in fibers under zero or low strain. The long period of the lamellar structure, estimated using correlation function analysis, increased with strain. Results from SAXS and WAXD analysis suggest that the formation of defects during yielding and plastic flow facilitates the α to β crystal phase transformation, and a phase, similar to conformationally disordered phase, whose density is close to that of crystal, is induced out of the amorphous phase in lamellar structure with application of strain.

Introduction

Poly(vinylidene fluoride) (PVDF) exhibits four crystalline forms, α, β, γ, and δ, which transform from one to the other under certain conditions.[1,2] The crystal structures of the four polymorphs, the intercorrelation among these forms, and its piezo- and pyroelectric properties have been the subject of many investigations,[3−11] which were reviewed thoroughly by Lovinger[1] and by Kepler and Anderson.[2] Among the four polymorphs, the α-form is obtained by quiescent crystallization from the polymer melt[4−6] and has a pseudoorthorhombic unit cell with a = 4.96 Å, b = 9.64 Å, c = 4.62 Å, and β = 90°. The β-form, which is the molecular origin of its most celebrated application as piezo- and pyroelectric material, can be obtained by cold drawing of the α-form film[3−5,8,12] and has an orthorhombic unit cell with a = 8.58 Å, b = 4.91 Å, and c = 2.56 Å. Studies of the preparation of the β-form from the α-form by mechanical deformation have attracted many researchers. The α to β transformation mechanism was investigated experimentally by Matsushige et al.,[12] and they concluded that heterogeneous stress distribution in the sample played a critical role in crystal transformation. In a simulation of the α-relaxation of PVDF in the α-form, Carbeck and Rutledge[13] found that defect introduction in the α-crystal can trigger the α to β transformation. Most reported studies involve WAXD measurements on PVDF films, but studies on the α to β transformation in the fiber form have seldom been reported. We are interested in this transformation, because the uniaxial geometry in a fiber allows us to better understand the changes in structure (WAXD) as well as morphology (SAXS) during deformation.

SAXS is a useful tool to characterize polymer morphology.[14,15] SAXS studies on fibers of a large range of polymers have been reported,[16−20] and quantitative evaluation of SAXS data has been developed by Ruland,[21,22] Grubb,[17] and Crist.[19,20] However, 2-D SAXS patterns have rarely been recorded simultaneously with WAXD patterns during the α to β transformation of PVDF fiber. Thus, little knowledge on morphological change during this transition is available. Therefore, in this study, we have carried out in-situ simultaneous synchrotron WAXD and SAXS measurements to investigate PVDF fibers during stretch−hold deformation. The effects of strain and take-up speed on the α to β transformation and on the internal morphology are also investigated.

Experimental Section

SOLEF 6010/0001 PVDF pellets, produced by Solvay S. A., Brussels, Belgium, were used to spin fibers. This material has a melt flow index of 17 at 230 °C with no nucleating agent. The PVDF fibers were melt-spun at take-up speeds of 10.6, 28.6, 39.4, and 61.0 m/min and were annealed at room temperature for at least 72 h to allow the material to reach equilibrium.

Synchrotron X-ray measurement was carried out at the Advanced Polymers Beamline (X27C) of the National Synchrotron Light Source, Brookhaven National Laboratory (λ = 1.307 Å, monochromatized by a double-multilayer (silicon/tungsten) with an energy resolution of 1.1%, beam diameter

* To whom all correspondence should be addressed.

10.1021/ma990896w CCC: $19.00
Published on Web 02/12/2000

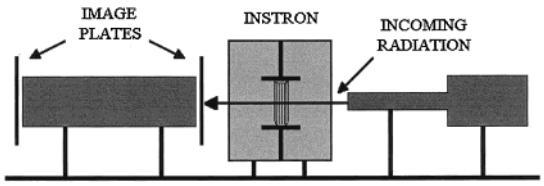

Figure 1. Experimental setup of WAXD/SAXS in deformation study.

= 370 μm). A schematic experimental setup is shown in Figure 1. The typical experimental procedure is illustrated as follows. A single filament of PVDF fiber, whose diameter is about 0.2−1 mm, is used to perform the scattering experiment. The PVDF fiber was stretched to a desired strain using an Instron stretching unit (model 4222) at a deformation rate of 5 mm/min and held at that strain for 2 min before the 2-D WAXD and SAXS scattering patterns were recorded simultaneously by two Fuji HR-V imaging plates. The imaging plates were digitized by a Fuji BAS 2000 scanner with a resolution of 100 μm for both WAXD and SAXS patterns. Then the fiber was stretched to the next strain level for further measurement. Precautions were taken to ensure that the fiber was vertical during the experiment. The WAXD imaging plates contained a central hole of 2.5 cm diameter to allow passage of the SAXS signal. The typical collection time for WAXD patterns was 1 min while that for SAXS patterns was 2 min. The recorded WAXD and SAXS patterns or their corresponding one-dimensional (1-D) extracted profiles were subject to background and scattering volume corrections. The stress−strain curves under the same experimental conditions were recorded separately off-line using a holding time of 5 min between two successive strains in order to simulate 2 min holding time and about 3 min scattering time during the scattering experiment. The repeatability of the results was found to be good.

Data Analysis

Typical WAXD and SAXS scattering patterns for undrawn fibers are shown in Figure 2a and Figure 3a, respectively. Data analysis will be demonstrated for these two patterns. For comparison purposes, all the WAXD and SAXS scattering patterns are grouped in pairs and are shown in Figures 4 and 5 for fibers at zero strain and in Figures 7−9 for fibers under deformation. All these patterns are analyzed in precisely the same manner as demonstrated. Note that Figure 2a and Figure 4a are exactly the same, as are Figure 3a and Figure 5b.

Unit Cell Parameters for α-Form WAXD. A typical 2-D WAXD pattern for undrawn fibers is shown in Figure 2a. Seven independent β-form reflections and 11 independent α-form reflections are observed. Indices were assigned to both α- and β-reflections as shown in Figure 2a. Note that some of the β-reflections overlap with the α-reflections, and their existence is confirmed by the peak deconvolution described in the next section. Eleven *d*-spacings of the α-form were used to determine the α-form unit cell parameters with a least-squares regression method. For overlapping reflections such as 110α/011α, equal weight fractions are assigned for each reflection during regression. The standard deviations for the calculated unit cell parameters are all less than 1.5%. Most of the error comes from the energy dispersion of the incident beam with an energy resolution of 1.1%, which gives rise to a relative error of 1.1% for the *d*-spacing measurement.

Overall Crystallinity Index From WAXD. The center on the WAXD pattern was first determined on the basis of the symmetry of the reflections before integration along the azimuthal direction from 0° to 360° for all diffraction angles (2θ) was carried out. The integrated value at a given diffraction angle was then normalized by the number of pixels contributing to the integration. The resultant profile was similar to a usual X-ray powder diffraction pattern (intensity vs diffraction angle (2θ)) and will be termed a powder curve. This curve was then deconvoluted into individual indexed peaks and amorphous halo using the Levenberg−Marquardt method.[25] The peak type was chosen to be Gaussian, and the position of the maximum of the amorphous halo is confined to an angular region of maximum width of 0.8°. The overall crystallinity index is given by the following formula:[15]

$$\text{crystallinity index} = \frac{A_c}{A_c + A_a} \tag{1}$$

where A_c and A_a are the sum of areas under the crystalline and amorphous peaks, respectively. A portion of the powder curve for Figure 2a is shown in Figure 2b. The deconvoluted constituent peaks are shown as well.

It is noted that crystallinity calculations for the 2-D WAXD patterns from oriented samples have seldom been reported. The most correct method to access the crystallinity of an oriented system can be obtained by the full reciprocal space method of Ruland and Dewaelheyns.[23] If the contribution of the missing meridianal peaks after the spherical averaging correction is small, the above-described method may approximate the true crystallinity. Furthermore, we believe the difference between the calculated and the true crystallinity will be consistent between the images, and the result can be used for comparison purposes.

SAXS Analysis To Calculate the Dimensions of Lamellar Morphology. A typical 2-D SAXS pattern from undrawn fibers, spun at 61.0 m/min, is shown in Figure 3a where two-lobe patterns at the first layer line position can be observed. This indicates the existence of a stacked lamellar structure. As will be discussed in the Results section, the morphology of the fiber spun at 61.0 m/min will be described by an irregular stacking of irregular lamellae within a microfibril.

The correlation function ($\gamma(r)$) analysis method[24] is adopted to quantitatively analyze the lamellar structure. For this analysis, a projection operation is first applied to obtain the integrated intensity on the meridian ($I_1(q_3)$) using the following formalism:

$$I_1(q_3) = \int_0^\infty I(q_{12},q_3) q_{12}\, \mathrm{d}q_{12} \tag{2}$$

where $q = 4\pi \sin\theta/\lambda$ is the scattering vector. The subscript 3 represents the meridianal direction, and the subscript 12 represents the equatorial direction. To obtain scattering intensity profiles solely from the lamellar structure, the intensity in a rectangular region, whose height just covers the beam stop, is set to zero to exclude scattering from the beam stop and microvoids before the projection operation is performed. This operation is illustrated in Figure 3b.

After obtaining $I_1(q_3)$, a 1-D Fourier transformation is then applied to it to obtain the correlation function.

$$\gamma(x) = \int_0^\infty I_1(q_3) \cos(q_3 x)\, \mathrm{d}q_3 \tag{3}$$

By using the method proposed by Strobl and Schneider[24] and by assuming a lamellar two-phase morphology, the

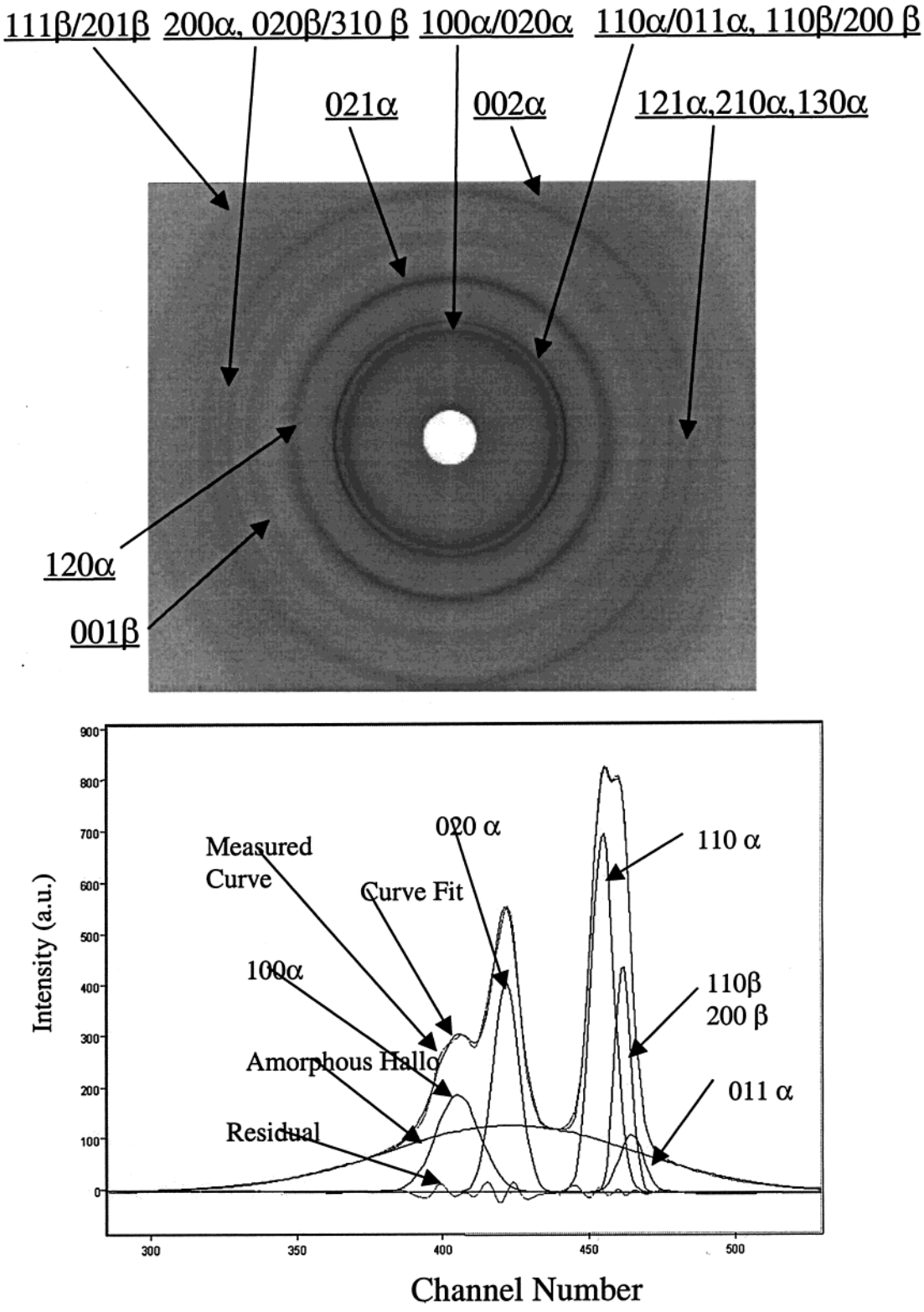

Figure 2. WAXD patterns for undrawn fiber: (a, top) fiber spun at 10.6 m/min, (b, bottom) a portion of the corresponding 1-D powder curve.

long period, L, and the lamellar and amorphous layer thicknesses can be estimated. The invariant or the value of $\gamma(0)$ can also be obtained from the correlation function.

Microfibril or Microvoid Length Estimation. For high take-up speed fiber at zero or low strain, as shown in Figure 3a, the existence of an equatorial streak indicates density fluctuations across the fiber. As will be shown in the Results section, this equatorial streak represents microfibrils separated by thin amorphous gaps in the fiber. For both high and low take-up speed fibers at high strain, another kind of equatorial streak is observed, as shown in Figures 7b, 8b, and 9b. Again, as will be shown in the Results section, this kind of scattering streak is attributed to microvoids generated by stretching. To estimate the microfibril or microvoid length, the method established by Crist[19,20] is adopted.

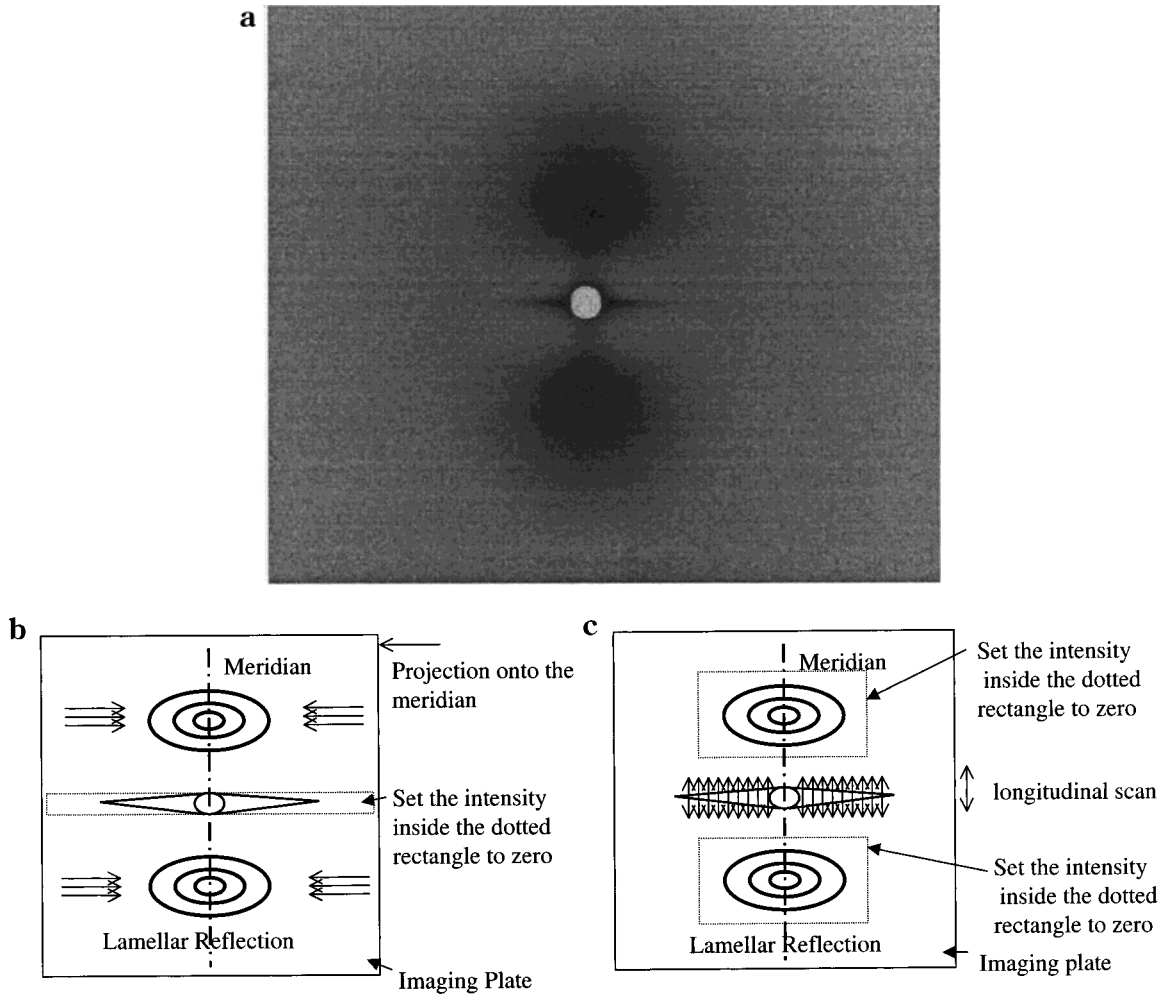

Figure 3. SAXS patterns for undrawn fiber: (a) fiber spun at 61.0 m/min, (b) corresponding diagram for correlation function analysis, (c) corresponding diagram for estimation of microfibril or microvoid length.

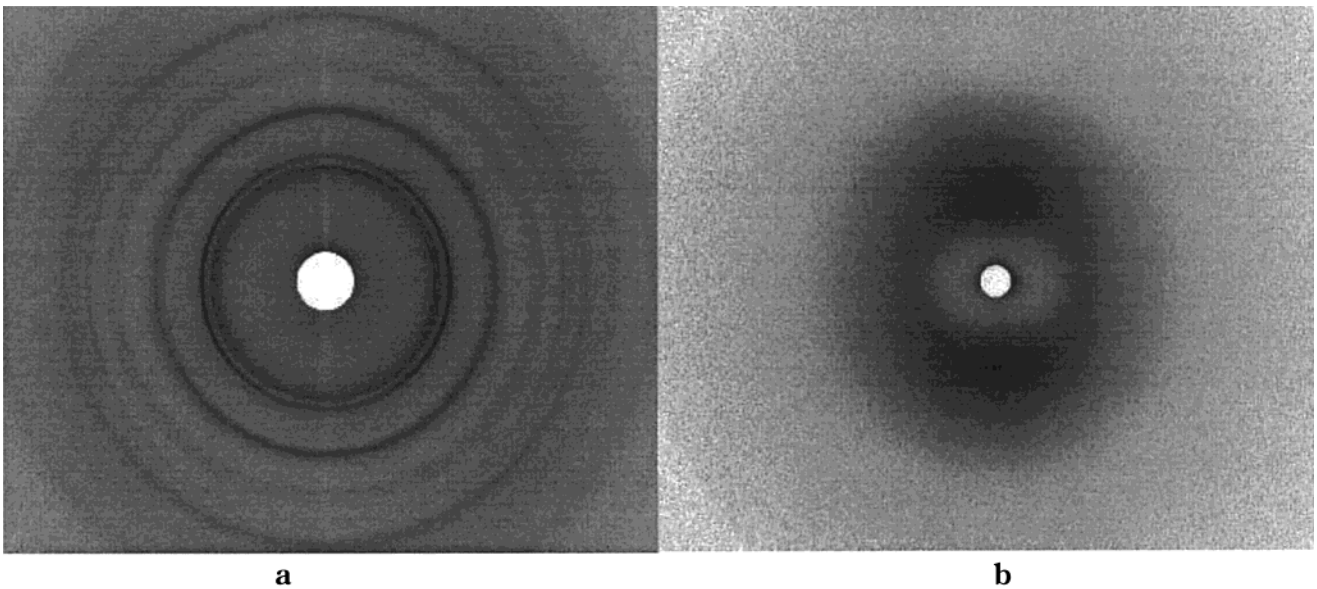

Figure 4. Scattering patterns for undrawn fiber spun at 10.6 m/min: (a) WAXD pattern, (b) SAXS pattern.

As shown in Figure 3c, the lamellar reflections were first set to zero before longitudinal scans of the equatorial streak were taken perpendicular to the equator. These sliced profiles were fitted with Lorentzian functions. The integral breadths (IB) of these fitted peaks were found to increase with the scattering vector component q_{12} and can be fitted to the following equation,[17]

$$\frac{(\mathrm{IB})^2 \cos(2\theta)}{\lambda D} = \frac{1}{2l_{\mathrm{f,v}}} + \left[\frac{1}{4l_{\mathrm{f,v}}} + \frac{{q_{12}}^2 \sin^2 \beta_{\mathrm{f,v}}}{4\pi^2}\right]^{1/2} \quad (4)$$

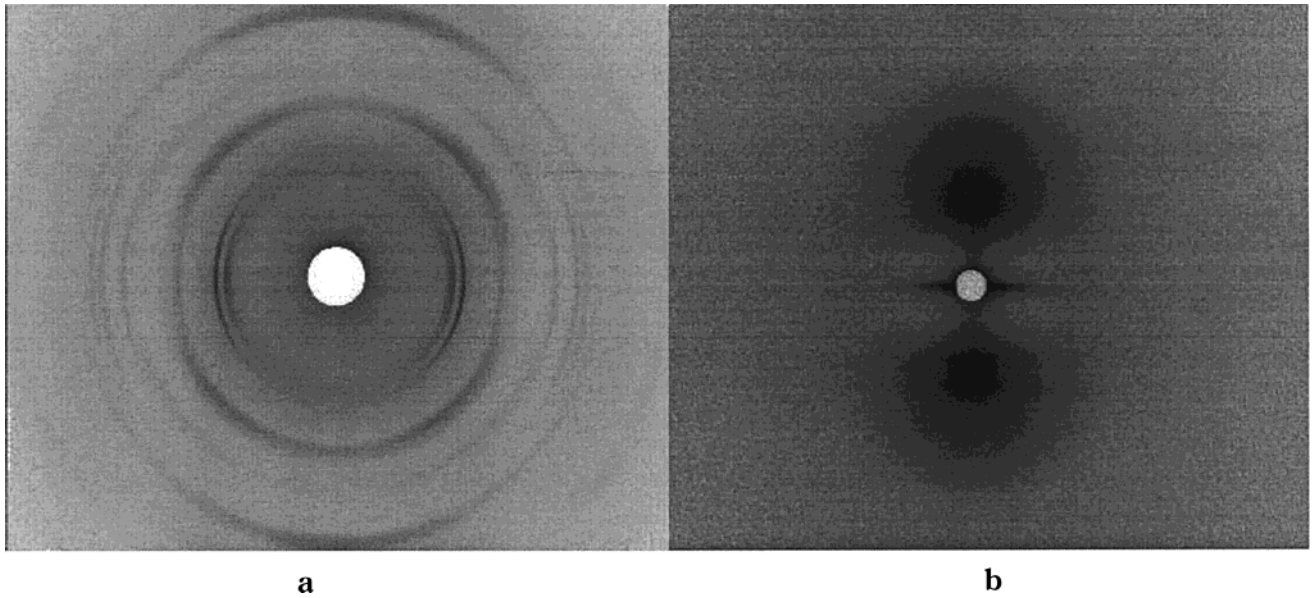

Figure 5. Scattering patterns for undrawn fiber spun at 61.0 m/min: (a) WAXD pattern, (b) SAXS pattern.

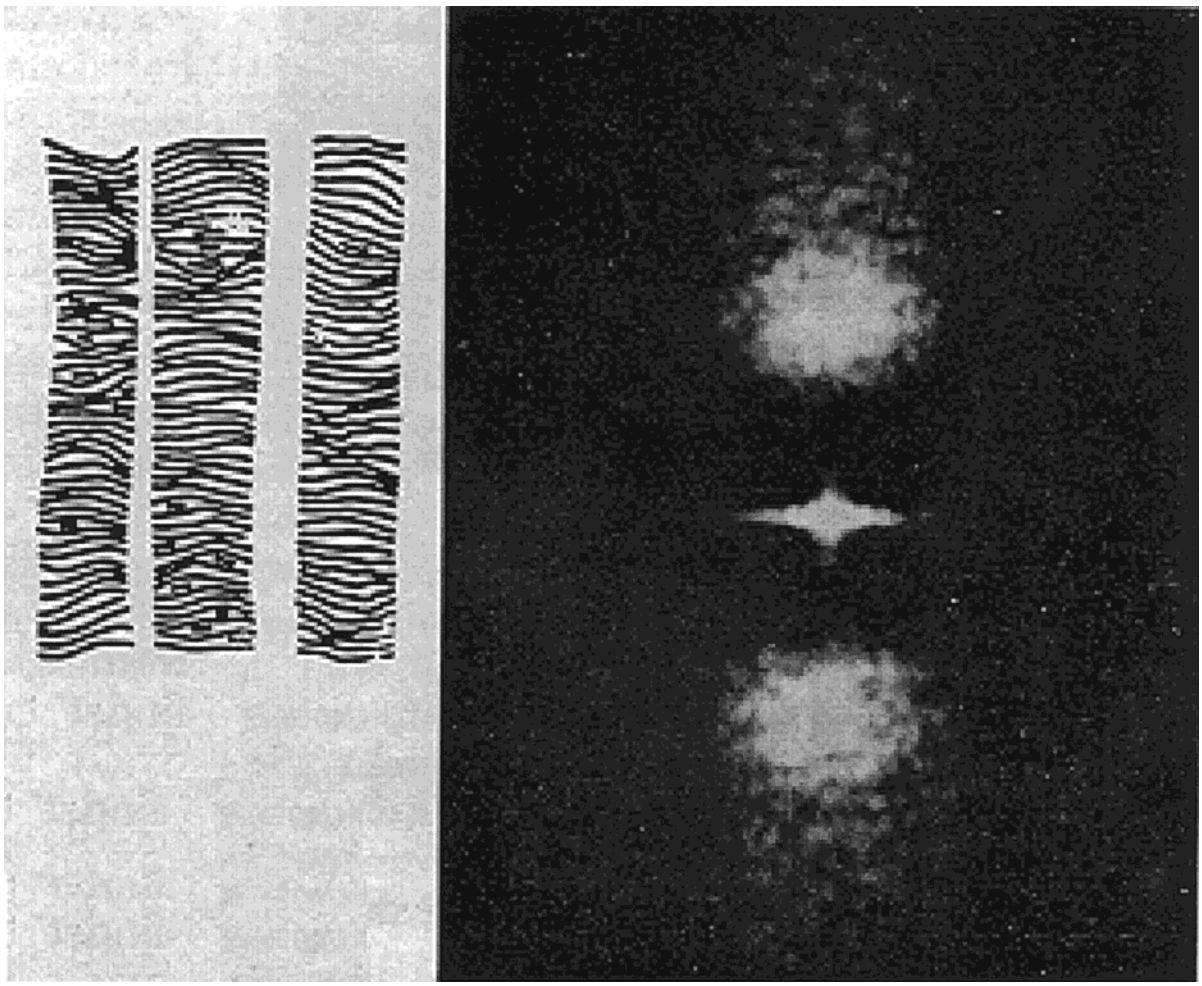

Figure 6. Scattering pattern generated by arrays of paracrystalline stacks (from ref 30, Abb. 5).

$q = 4\pi \sin \theta/\lambda$ is the scattering vector and q_{12} is its component in the equatorial direction, 2θ is the scattering angle, λ is the wavelength of the X-ray, D is the sample−detector distance, $l_{f,v}$ is the length of the microfibrils or microvoids, and $\beta_{f,v}$ is the misorientation factor of the microfibrils or microvoids. The length, $l_{f,v}$, and the misorientation factor, $\beta_{f,v}$, of the microfibrils or microvoids can be obtained by a nonlinear fit of IB vs q.

It is noted that deconvolution of the beam profile was not performed for the longitudinal scans of the equatorial streak because the beam size is so small that the scattering can be regarded as from a point source.

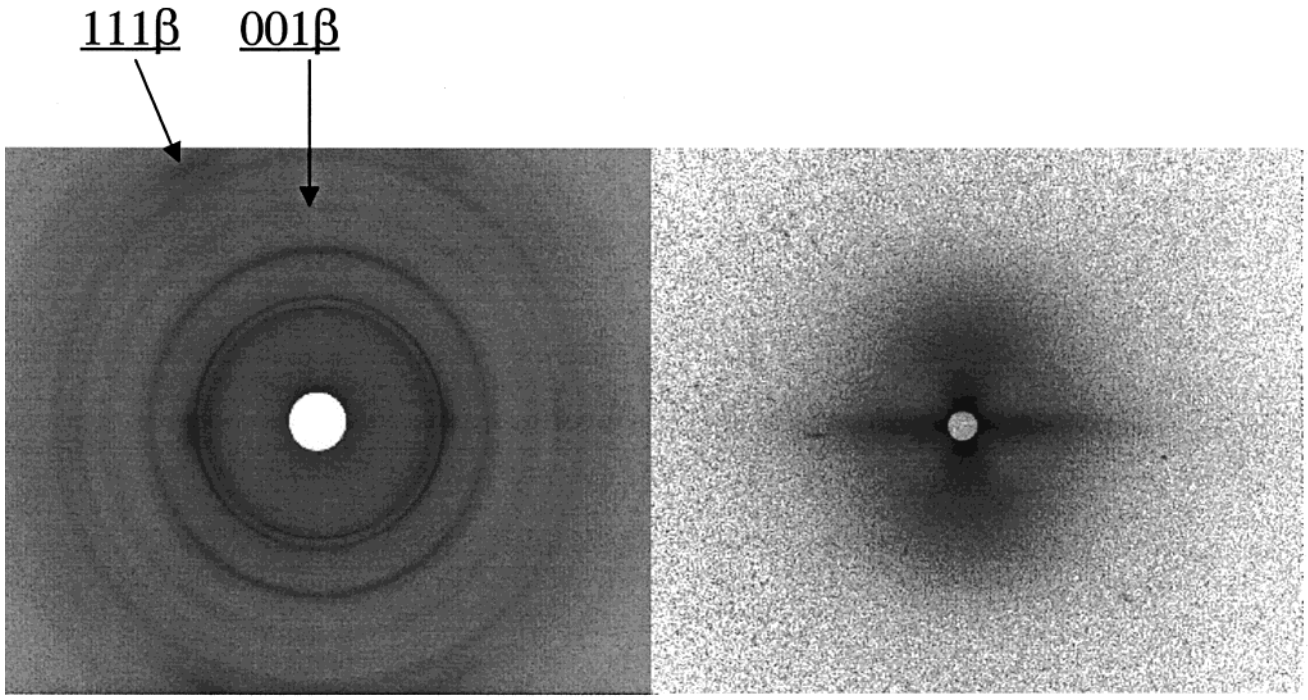

Figure 7. Scattering patterns from unnecked regions of fiber spun at 10.6 m/min at strain of 70%: (a) WAXD patterns, (b) SAXS patterns.

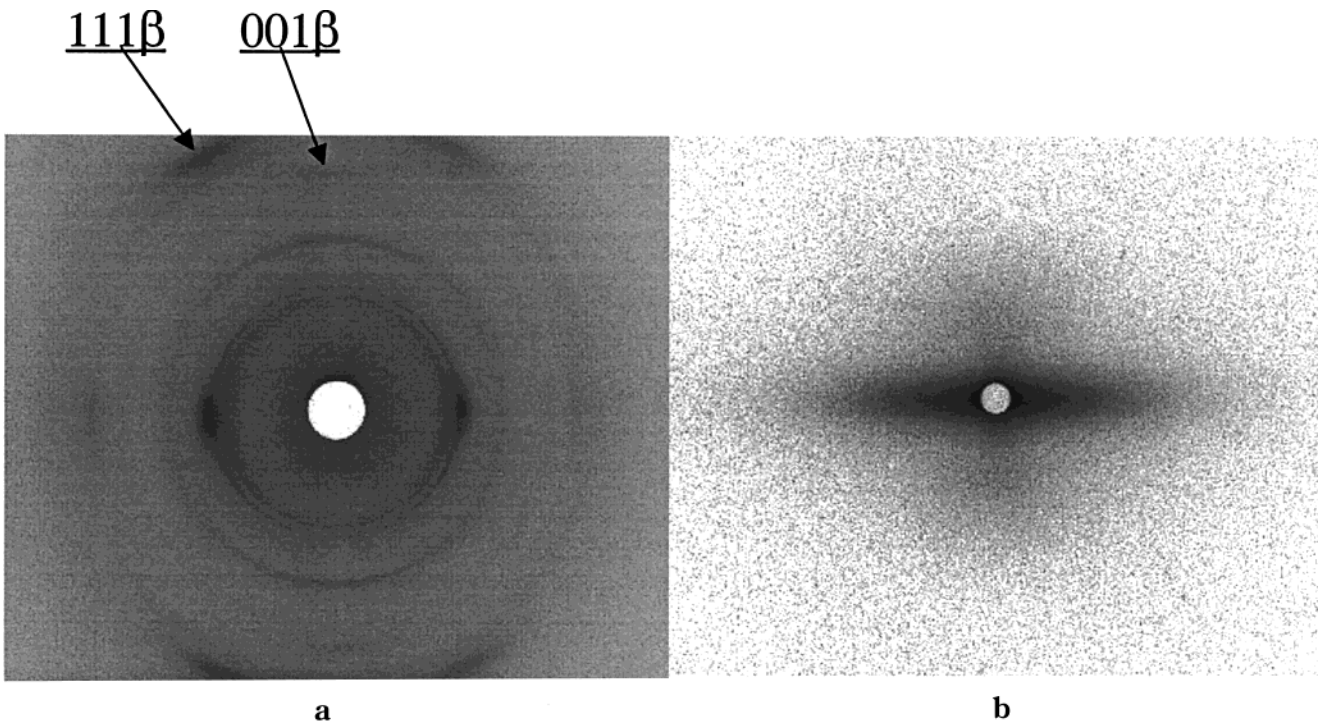

Figure 8. Scattering patterns from necked regions of fiber spun at 10.6 m/min at strain of 60%: (a) WAXD patterns, (b) SAXS patterns.

Results

Qualitative Observations on Scattering Patterns and Morphology Identification. For undrawn fibers, WAXD patterns (Figures 4a and 5a) show a transition from rings to arcs, indicating that the crystalline orientation increases with take-up speed. This observation is consistent with the corresponding SAXS signal shown in Figures 4b and 5b in which the shape of meridianal arcs transform into lobes, suggesting that the orientation of the lamellae also increases with take-up speed.

As shown in Figure 5b, an azimuthally narrow equatorial streak is evident at zero or low strain for the high take-up speed of 61.0 m/min. The shape of this SAXS pattern is intriguing and in fact carries considerable qualitative information about the morphology of the system. The lobes observed along the meridian suggest Bragg scattering from a periodic system of

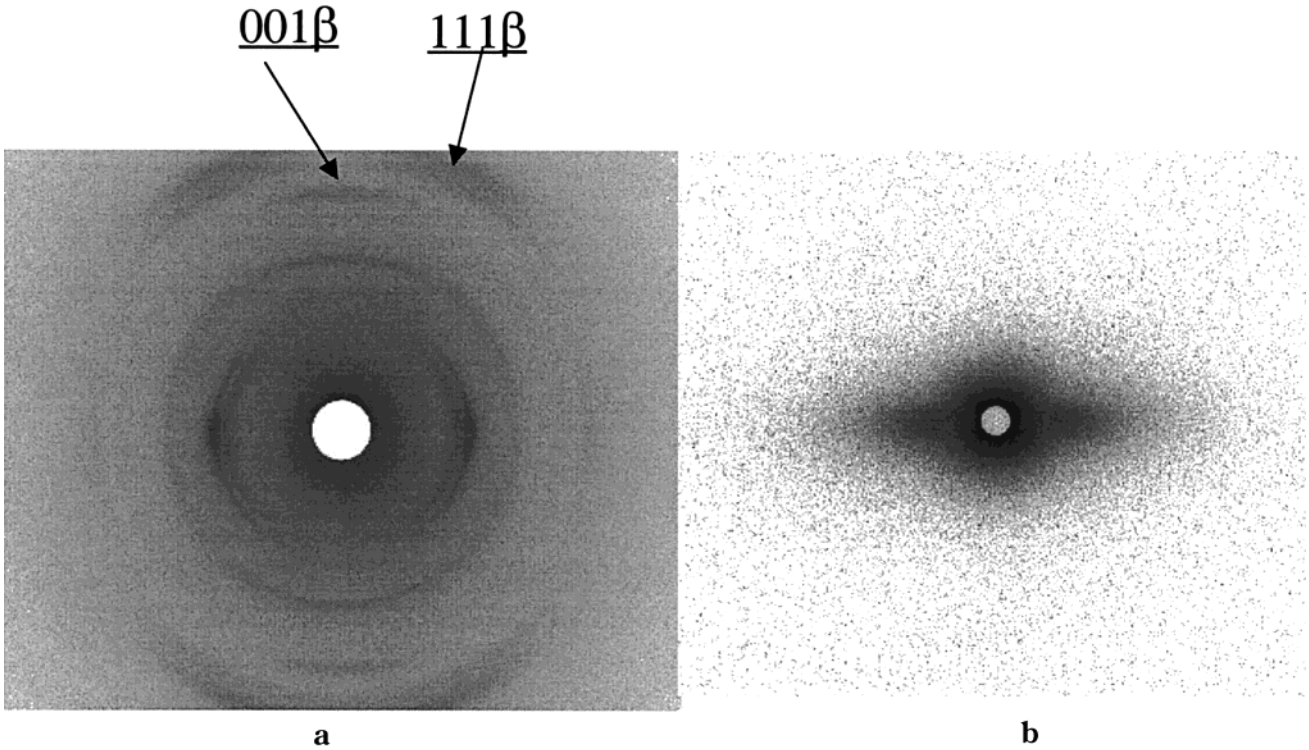

Figure 9. Scattering patterns from necked regions of fiber spun at 61.0 m/min at strain of 140%: (a) WAXD patterns, (b) SAXS patterns.

alternating crystallites and noncrystalline regions—a classical "row structure".[26] A perfectly periodic stacking would produce perfectly sharp peaks at $q = 0$ and at each Bragg position $q = \pm 2\pi n/L$, where n is an integer and L is the periodicity or long spacing.[27] This is not what is observed in Figure 5b. What is seen there is a thin equatorial streak, bloblike first-order meridianal peaks and no trace of a second-order SAXS peak. This kind of behavior is possible only if the stack of crystallites gradually loses long-range order; that is, the stacking is "paracrystalline".[28,29] This situation was recognized in the early 1960s by Bonart and Hosemann. Figure 6 is a remarkable illustration from their 1962 work.[30] At the left of the figure they show such a paracrystalline array: three narrow stacks (microfibrils), each composed of irregularly curved black stripes (simulating lamellar crystallites), both crystallites and microfibrils separated by blank regions (amorphous phase), with the stripe stacking gradually losing long-range order. This sketch was converted into a diffraction mask. Light scattering from the mask is shown on the right. The general features of this diffraction pattern are identical to those of Figure 5b: a thin equatorial streak, bloblike first-order peaks, and no higher-order diffraction. This irregular stacking of irregular lamellae within a microfibril is taken to describe the morphology of the fibers spun at 61.0 m/min. We will term the streak in Figure 5b an equatorial streak of the first kind.

The absence of an extended equatorial streak in SAXS pattern Figure 4b for the fiber spun at 10.6 m/min indicates that the lamellae are wide normal to the fiber axis. The curvature of the SAXS Bragg arc indicates substantial misorientation of the lamellar normals with respect to the fiber axis.

The morphological behavior observed in Figure 5b is to be compared with what is observed at higher macroscopic strains. WAXD and SAXS patterns from unnecked and necked regions at high strains are shown in Figures 7−9. The SAXS patterns are the (b) parts of these figures. We observed that a broader and more intense equatorial streak is recorded at high strains in both necked and unnecked regions for both high and low take-up speed fibers. This streak will be termed an equatorial streak of the second kind. If numerical values are compared, the recorded intensity of equatorial streak of the second kind appears similar to that of the first kind, but only because the time of registration for the second kind of equatorial streak is about 1/20 of that of the first kind of equatorial streak. The equatorial streak of the second kind is attributed to microvoid formation while the former is attributed to the morphology of the microfibrils. Our justifications to this conclusion are as follows. Since the SAXS signal is produced by electron density inhomogeneity in the sample, the scattering intensity is proportional to the square of the density difference between the constituting phases. If the densities of the crystalline, amorphous, and microvoid regions of PVDF are approximately 1.953,[32] 1.619,[33] and 0 g cm^{-3}, respectively, the scattering intensity due to the crystallite and microvoids domains would be about 30 times stronger than that due to crystallite and amorphous phases. A similar situation has been observed in our experiment. During our experiment, the streak signal of the high-strain sample saturates the imaging plate detector for only 10 s of exposure time, while the other streak signal from the low-strain sample cannot saturate the imaging plate even after 2 min collection time. This perhaps justifies our preliminary assignment of voiding to the equatorial streak at high strains and of crystal−amorphous density differences at no or low strains for high take-up speed fibers.

Fiber Appearance and Stress−Strain Curves. The stress−strain curve for the fiber spun at 10.6 m/min during the stretch−hold operation is shown in Figure 10. For fibers spun at other speeds, the stress−strain behavior is very similar to that shown in Figure 10. In

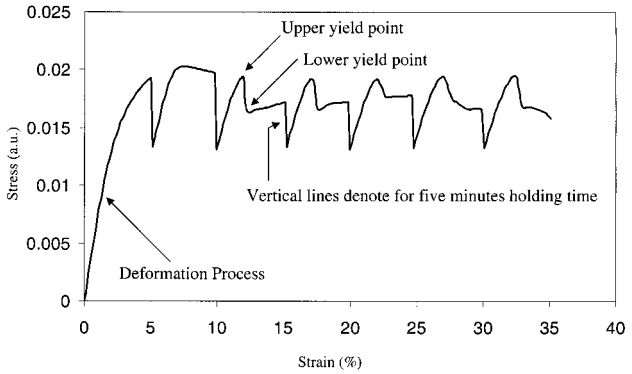

Figure 10. Stress−strain relationship for fiber spun at 10.6 m/min.

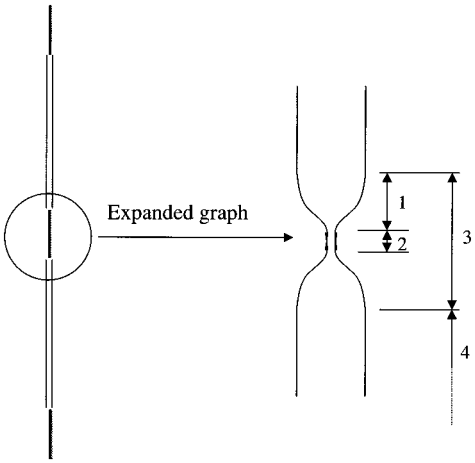

1. Shoulder: transition from un-necked to necked region
2. Neck
3. Necked region: shoulder + neck, 2-3 mm
4. Un-necked Region: 10-20 mm

Figure 11. Schematic diagram for the appearance of the yielded fiber.

this figure, it is observed that the fiber yields at about 5%−10% strain, and the curve exhibits an upper and a lower yield point. After yielding, necked and unnecked regions are developed alternately along the fiber, and the appearance of the fiber is sketched in Figure 11. As shown in Figure 11, the regions including shoulder and neck are short (about 2−3 mm), thin, and opaque, while the unnecked regions are thick, transparent, and long (about 10−20 mm). The combined length of shoulder and neck was so small that it was impossible to tell shoulder from neck during the experiment. We could only identify whether the scattering is from unnecked regions or not. Thus, in this paper, "necked region" is used to denote the region including both shoulder and neck.

It needs to be mentioned here that the stretch−hold deformation is nonsymmetric, and the detection point of the X-rays is actually moving. Since the unnecked region is much longer than the necked region, most data collected are from the unnecked region. It is assumed that the unnecked region is fairly uniform except for the part adjacent to the neck region. This assumption is reasonable because the unnecked region is fairly long, and the patterns taken at different spots of one unnecked region at a certain strain show no significant variation in crystallinity and long period. During the experiment, special caution is given to make sure data are taken in a place well inside in the unnecked region.

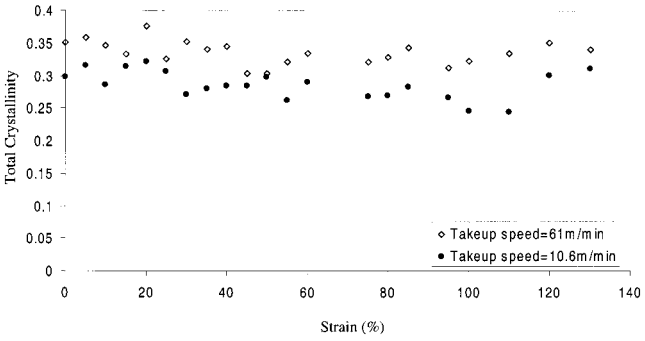

Figure 12. Bulk crystallinity index vs strain.

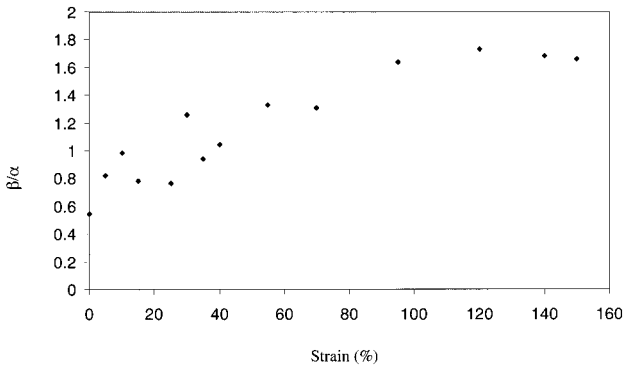

Figure 13. β to α ratio vs strain for unnecked regions of fiber spun at 10.6 m/min.

Some data points from necked region are also collected. However, since the necked region is very short, it is impossible to identify whether the data are taken at the neck or the shoulder.

It also has to be noted that the stress in Figure 10 is nominal because it is obtained by the load divided by the initial cross section of the fiber and that the stress in the necked region may be much greater than that in the unnecked region. Since the true stress is hard to determine and the stress distribution in the unnecked regions is different from that in the necked regions, macroscopic strain is used as a variable to express the extent of stretching in the unnecked region. The dependence of other physical quantities, such as crystallinity index, cell dimensions, and long period, etc., on the extent of stretching in the unnecked regions is expressed in terms of strain. Special notice will be given if the physical quantities are measured in the necked regions.

Bulk Crystallinity Index and β/α Ratio. The bulk crystallinity index vs macroscopic strain in an unnecked region of the fiber spun at 10.6 and 61.0 m/min is shown in Figure 12. For each strain increment beyond the yield strain (5%−10%), the initial increase in the macroscopic strain produces a temporary stress increase in the unnecked material as the crosshead movement is begun (see Figure 10), followed by additional time at the flow stress. Despite fluctuations, it is observed that the bulk crystallinity index is constant throughout the deformation. The ratio between the β and the α crystal forms (β to α ratio) in the unnecked region for fiber spun at 10.6 m/min is shown in Figure 13. The coexistence of both α and β (minor fraction) crystal forms in undrawn fibers has been illustrated in Figure 2b. It is thus clear that the α form is converted to the β form gradually with increasing strain. The ultimate level of the β/α ratio is 1.6 at large strains in the unnecked region. Since the total crystallinity does not change with strain, it appears

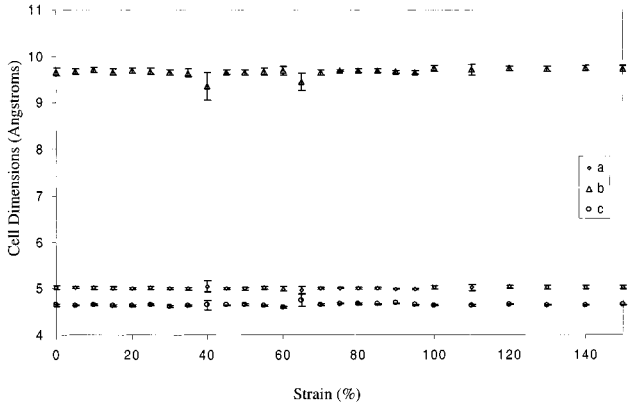

Figure 14. Unit cell dimensions vs strain for fiber spun at 10.6 m/min.

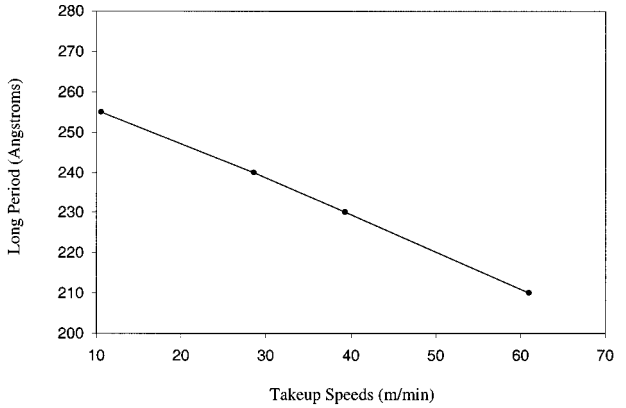

Figure 15. Long period vs takeup speeds for fibers at zero strain.

that the strain only induces the α to β transition, not crystallization. In the necked region, the ultimate β/α ratio is approximately 4, showing that the α to β transition is enhanced in the necked region. To the authors' knowledge, no quantitative results have been previously published on β/α ratios for PVDF films or fibers.

Unit Cell Dimension of the α Form. In the unnecked region, the unit cell dimensions of the α crystal form in fiber spun at 10.6 m/min are shown in Figure 14. It is observed that the cell dimensions of the α-form remain approximately constant with strain. This is also true for fiber spun at 28.6, 39.4, and 61.0 m/min.

Long Period of the Lamellar Structure. The dependence of the long period of the undrawn fiber on take-up speed is shown in Figure 15. It is seen that the long period decreases with increasing take-up speed. This is due to the fact that the faster the take-up speed, the larger the cooling rate. At the faster cooling rates, the degrees of supercooling during crystallization are increased, resulting in thinner crystals and shorter long periods. The relationships between the long periods in the unnecked region and the strain for fibers spun at 10.6 and 61.0 m/min are shown in Figures 16 and 17, respectively. For the low take-up speed (10.6 m/min) fiber, the long period increases gradually with increasing strain and reaches an asymptote at a strain of 45%. When strain is above 70%, no lamellar reflections on the meridian can be observed. In contrast, the long period of the high take-up speed fibers (61.0 m/min) shows an abrupt increase at a strain of 15% and remains constant after that. No lamellar reflection can be observed when strain is above 20%. The dependence

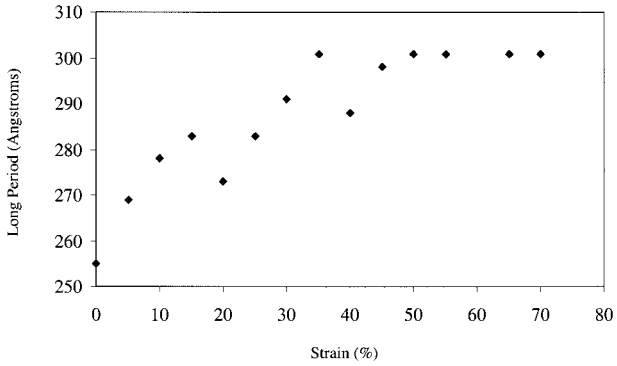

Figure 16. Long period vs strain for unnecked regions of fiber spun at 10.6 m/min.

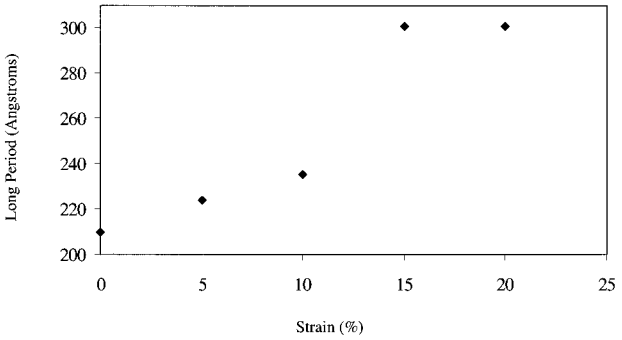

Figure 17. Long period vs strain for unnecked regions of fiber spun at 61.0 m/min.

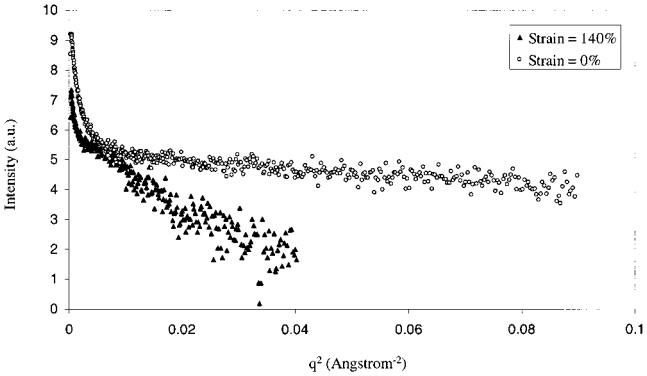

Figure 18. Equatorial intensity plotted versus q^2 for fiber spun at 61.0 m/min, strain = 0% and 140%.

of long period with strain will be further discussed with projected intensity in Discussion section.

Estimate of the Microfibril and Microvoid Length. As discussed before, the equatorial streaks observed at zero or low strain for high take-up speed fibers are attributed to microfibrils, while those observed at high strain for both low and high take-up speed fibers possibly originate from microvoids.

Figure 18 shows the equatorial intensity plotted versus q^2 for (a) the as-spun fiber using a take-up speed of 61.0 m/min and (b) the same fiber strained at 140%. The as-spun fiber shows a smooth decay in intensity, whereas a hump is observed in the stretched fiber. This hump is more prominent if the data are plotted in a Porod plot, as shown in Figure 19. The hump represents constructive interference between the long, thin microvoids aligned along the fiber axis. Application of Bragg's law suggests an intervoid spacing of approximately 8.0 nm.

To further analyze the equatorial SAXS data, it is necessary to determine whether the observed scattering

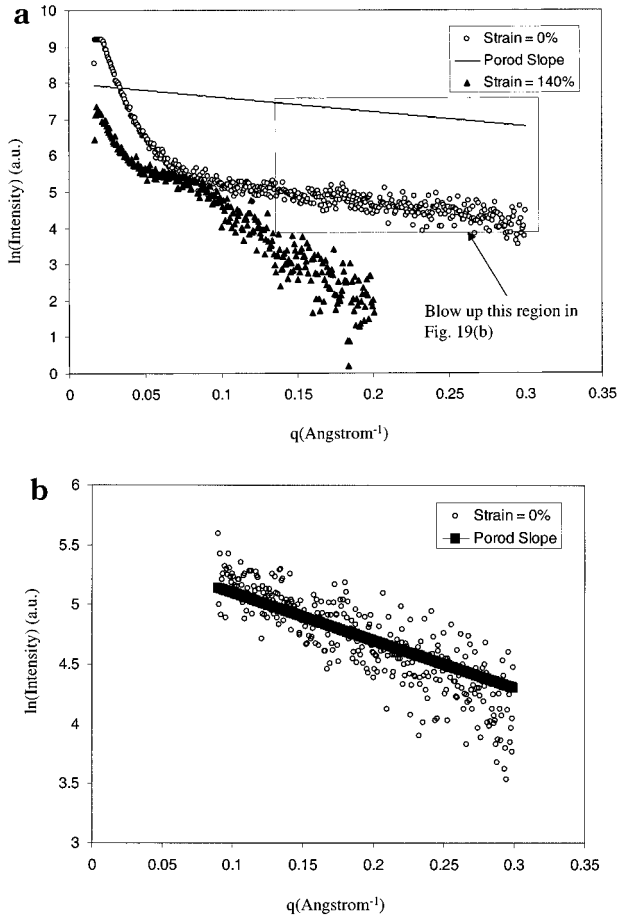

Figure 19. Porod plot for the data shown in Figure 18: (a) Porod plot for the whole data, (b) Porod plot for the data region marked by square in (a).

is in the tails of the scattering (the Porod) region or whether it is well inside the Porod region, allowing Guinier's law analysis. In the Porod region the intensity is proportional to q^{-4}. It is therefore useful to plot ln I against a slope of -4. This is done in Figure 19a,b for the two fibers of Figure 18. In this figure, it is seen that the equatorial scattering from the as-spun fiber is everywhere in the Porod region beyond $q = 0.08$ Å^{-1}, while the scattering of the drawn fiber has not yet reached the Porod slope. Thus, it is reasonable to attempt fitting the scattering of the drawn fiber to Guinier's law, plotting ln I vs q^2.

For the drawn fiber in Figure 18 a short region (up to $q^2 = 0.006$) shows a steeply descending intensity. Beyond this region, the data fall on a straight line. Figure 20 is a Guinier plot of these data. Using the relationship for rodlike scatterers,[31]

$$\ln I = \text{const} - \frac{q^2R^2}{4} \qquad (5)$$

one identifies a diameter of 1.89 nm for these microvoids.

The length of the microfibril or the microvoid can be estimated by fitting the integral breadth of the longitudinal scan of the equatorial streak using eq 4. The integral breadths and the fitted curves for microfibrils and microvoids are shown in Figure 21 and Figure 22, respectively. No significant equatorial streak resulting from microfibril scattering is observed above 10% strain. The microfibril length for strain 0%, 5%, and 10% ob-

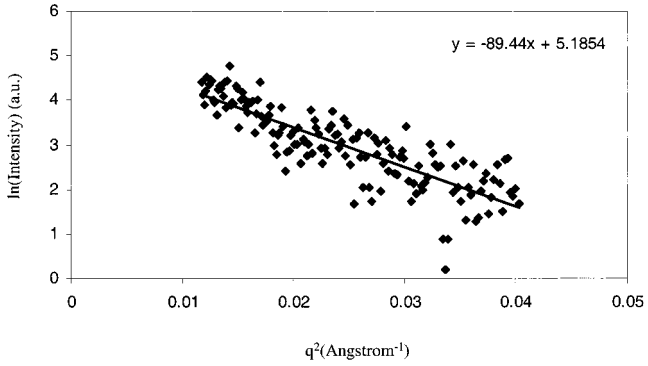

Figure 20. Guinier plot for drawn fiber to determine the diameter of microvoids (take-up speed = 61.0 m/min).

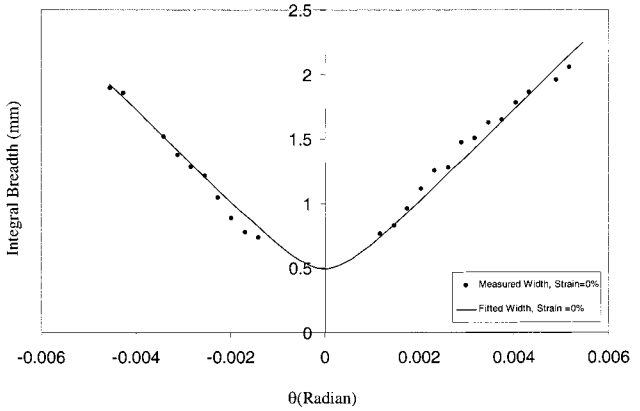

Figure 21. Integral breadth of equatorial streak vs scattering angle (θ) in the SAXS pattern taken from unnecked region of fiber spun at 61.0 m/min, strain = 0%. The scattering entity is microfibrils.

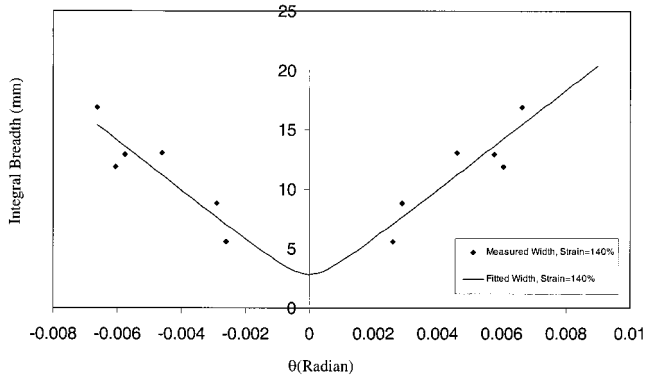

Figure 22. Integral breadth of equatorial streak vs scattering angle (θ) in the SAXS pattern taken from unnecked region of fiber spun at 61.0 m/min. The scattering entity is microvoids.

tained from Figure 21 is constant, at about 400 nm. The misorientation factor for microfibril vs strain up to 10% is plotted in Figure 23. A constant level of fibrillar misorientation is observed up to at least 5% strain. By 10% strain, the misorientation has doubled. The increase in misorientation likely indicates local yielding and plastic flow.

The length of the microvoids estimated from Figure 22 is on the order of 70 nm.

In summary, using the above method, the dimensions of microfibrils and microvoids can be estimated. The diameter of microvoids is estimated to be around 2 nm with a length of 70 nm and an intervoid spacing of 8 nm. For microfibrils, only the length can be estimated

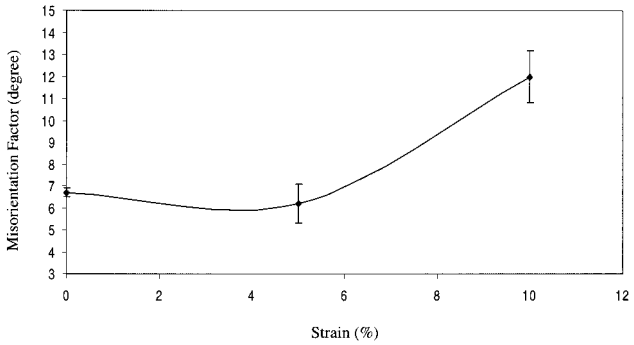

Figure 23. Misorientation factor vs strain at unnecked regions of fiber spun 61.0 m/min.

to be 400 nm. The misorientation factors for microfibrils are also extracted.

Discussion

Strain Effect on Lamellar and Fibrilar Structure. As shown in Figures 16 and 17, the long period increases gradually with increasing strain and levels off at about 45%−50% strain for the low take-up speed (10.6 m/min) fiber. This trend exists up to 70% strain. The long period shows an abrupt increase at a strain of approximately 15%, and there is no lamellar structure when strain is over 20% for the higher take-up speed (61.0 m/min) fiber. For both cases, it is observed that long period converges to about 300 Å. The long period increase may be due to extension of the chains in the amorphous layers between crystalline lamellae. With application of strain, the density in the amorphous region may increase due to close packing of amorphous chains. The density difference between crystalline and amorphous regions diminishes. Thus, lamellar reflection disappears at 70% strain and at 20% strain for fiber spun at 10.6 and 61.0 m/min, respectively. As shown in the previous section, the lamellae in fiber spun at 10.6 m/min are less oriented than those in fiber spun at 61.0 m/min. The sudden jump in the long period of fiber spun at 61.0 m/min at 15% strain may be due to nearly complete extension of less entangled, relatively oriented amorphous chains. The limiting long period of 300 Å may be characteristic for a stressed PVDF system. This conclusion may be supported by meridianally projected intensity plots shown in Figure 24a,b and the constant crystallinity results shown in Figure 12. In parts a and b of Figure 24, logarithm plots of meridianally projected intensity at different strains are shown for fiber spun at 10.6 and 61.0 m/min, respectively. This projected intensity is obtained using the formalism presented in Figure 3b. Note that before projection the equatorial intensity is set to zero; thus, this projected intensity denotes the density fluctuation along the fiber. From both parts a and b of Figure 24, it can be observed that the intensity of the meridianal reflection diminishes with increasing strain and finally disappears. This suggests that the density fluctuation along the fiber decreases and then vanishes. Since the crystallinity stays constant with strain, the only explanation we can see for this is that the amorphous chains are more and more closely packed together with increasing strain, and the density of the amorphous region approaches that of a crystal. The amorphous phase at this stage is somewhat similar to the hexagonal phases or conformationally disordered crystal suggested by Clark and Muus[34,35] and by Wunderlich and Grebowicz.[36] The

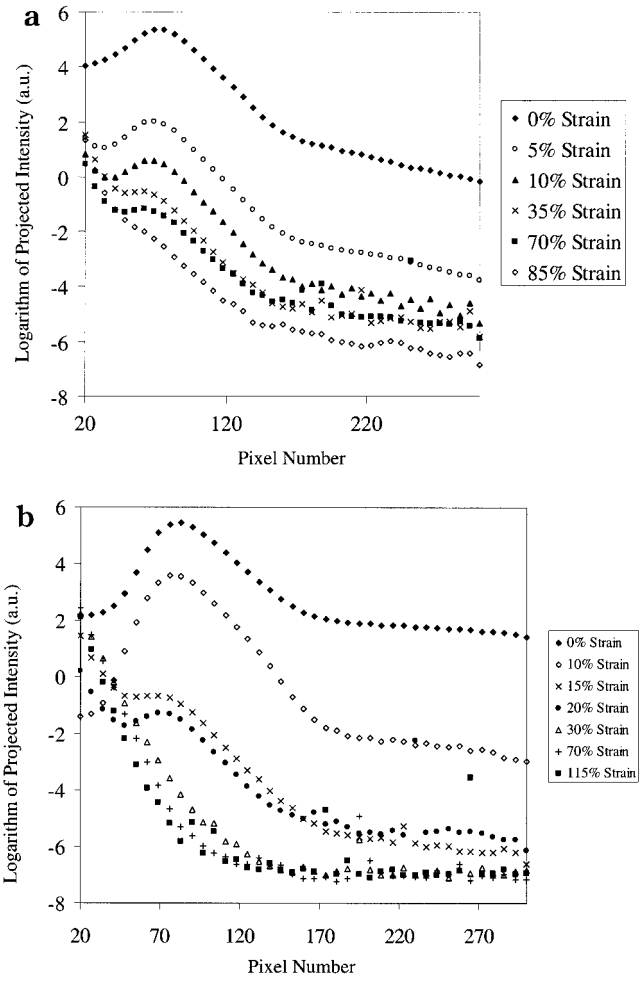

Figure 24. Logarithm plot of meridianally projected intensity at different strains (a) for fiber spun at 10.6 m/min and (b) for fiber spun at 61.0 m/min.

difference is that the amorphous phase at this stage is much less ordered and cannot produce crystalline reflections. The free volume produced by the close packing of amorphous chains is essentially responsible for the microvoids formed during stretching. This may be what happens at intermediate strains, 70% and 20% strain for 10.6 and 61.0m/min take-up speed, respectively, for the unnecked part of the fiber. At these strain levels, the crystalline phase is believed to begin to shear apart.

It is likely that the α crystallites begin to deform into small crystallites and some to convert into the β form at high strains, above 70% and above 20% strain for 10.6 and 61.0m/min take-up speed, respectively, for the unnecked part of the fiber. The lamellar structure is destroyed, as the crystals shear apart and the amorphous chains become extended and closely packed. Crystallites of α and β form and extended amorphous chains coexist with elongated microvoids. The density inhomogeneity at a relatively small length scale exits not only across the fiber (void) but also along the fiber (alternating mixed small crystallites of α and β form and amorphous chains). Thus, both an equatorial streak and a meridianal streak are observed, as shown in Figures 7b, 8b, and 9b.

For the necked part of the fiber, what happens at high strain at the unnecked parts is believed to take place during the yielding stage, 5% to 10% strain.

The α to *β* Transformation Mechanism. For drawn fibers (Figures 7−9), the reflections from the *β* crystal form (001 and 111) become evident after drawing. Since the bulk crystallinity remains about constant, this suggests that the crystal transition from α to *β* is induced by the application of strain. It is also observed that the crystals are more orientated in the necked regions than in the unnecked regions.

Matsushige et al.[12] have studied the α to *β* transformation by performing WAXD simultaneously with a tensile experiment. They reported that their PVDF sample necked upon stretching at room temperature and that the α to *β* transformation was observed by WAXD at the necked region. At temperatures above 140 °C, the sample deformed uniformly, no necking was observed, and no α to *β* transformation occurred. Thus, they concluded that heterogeneous stress distribution in the sample played an important role in the crystal transformation. However, no WAXD data on unnecked regions of the necked sample have been reported by them.

It was shown in this study that the α to *β* transformation occurs in both necked and unnecked regions. The only difference is that the extent of the transformation is larger in the necked region than in the unnecked region. It is reasonable to assume that the stress distributes rather uniformly in the unnecked region of the fiber. This conflicts with the proposed role of the heterogeneous stress distribution during the α to *β* crystal transformation.

Our results suggest that microscopic yielding occurs prior to the macroscopic yielding. Macroscopic plastic flow is implemented via necking. Microscopically, plastic flow refers to the fact that crystallites have been ruptured and sheared apart by the external force. In the necked regions of PVDF fiber, plastic flow takes place to such an extent that crystallite rupture is frequent, and the sample cannot maintain its macroscopic geometry. On the other hand, in the unnecked regions of PVDF, the localized breakage and slippage may take place in crystallites without causing the necking phenomenon. This is supported by the misorientation factor of microfibrils in the unnecked region of fiber spun at 61.0 m/min as shown in Figure 23. A constant level of fibrillar misorientation is observed up to at least 5% strain. By 10% strain, the misorientation has doubled. The increase in misorientation indicates local yielding and plastic flow.

The molecular simulation work of Carbeck and Rutledge[13] shows that defects in the α crystals facilitate the α to *β* transformation. In light of this result, we suggest that necessary defects are introduced during the crystallite breakage and yielding and that plastic flow in either necked regions or unnecked regions facilitates α to *β* crystal transformation. The upper yield point in the stress−strain curve represents the stress needed to destroy the α crystallites, while the lower yield point is the stress at which the transformed or partially transformed crystallites (*β* form) begin to slip. Since the yielding is global in the necked region and the concentration of defects created is much greater than that produced in the unnecked region where only local yielding and plastic flow take place, the residual α form in the necked region decreases to only about 20% of the total crystallinity, whereas about one-third of the total crystallinity in the unnecked region remains in α crystal form.

The above hypothesis is also supported by the constancy of the α unit cell dimensions during deformation. If the defects were to accumulate in α-crystals gradually during deformation or through aging under stress, the *a* and *b* lattice constants should measurably increase. This is not observed. This suggests that if defects are produced, they must be created during the initial stages of destruction of the α crystallites. We suggest that substantial internal rotation of the chain begins to take place at defects, where the interchain interaction is relatively weak, and this facilitates the transformation of chain conformation from the $TGT\bar{G}$ (α) form to the all-trans (*β*) form. In other words, creation of defects during the crystallite breakage may be an important path for the α to *β* crystal form transformation to take place.

At temperatures above 140 °C, although more defects may be easily created than the situation at room temperature, chain mobility is also higher, resulting in recrystallization to form the kinetically favored α form. This may explain why Matsushige et al.[12] did not observe any α to *β* transformation in their tensile experiment above 140 °C.

Conclusions

Our results suggest that the defect formation induced by yielding and plastic flow is important to produce the α to *β* crystal transformation in PVDF. In PVDF fiber, the α and *β* crystals coexist in a lamellar morphology. At high take-up speed, these lamellae form microfibrils. For the unnecked part of the fiber, at the molecular level, the application of stress at room temperature creates defects during the shearing of α crystals and thus facilitates the transformation of α crystals to *β* crystals, while at the morphological level, at intermediate strain, the extension of chains may assist the amorphous phase transformation into what is similar to a conformationally disordered phase and promote formation of microvoids. At high strains, crystallites are believed to be sheared apart. And the morphology is that of crystallites (mixed α and *β* form), linked by extended amorphous chains along the fiber axis and coexisting with the relatively strongly correlated microvoids.

Acknowledgment. We gratefully acknowledge financial support by NSF GOALI Grant DMR-9629825. Additionally, B.C. and B.H. acknowledge the financial support in part by grants from Army Research Office (DAAG 55971002, DAAG559710080).

References and Notes

(1) Lovinger, A. J. In *Development in Crystalline Polymers 1*; Bassett, D. C., Ed.; Applied Science: London, 1982; p 195.
(2) Kepler, R. G.; Anderson, R. A. *Adv. Phys.* **1992**, *41* (1), 1.
(3) Lando, J. B.; Olf, H. G.; Peterlin, A. *J. Polym. Sci., Part A-1* **1966**, *4*, 941.
(4) Hasegawa, R.; Kobayashi, M.; Tadokoro, H. *Polym. J.* **1972**, *3*, 591.
(5) Hasegawa, R.; Takahashi, Y.; Chatani, Y.; Tadokoro, H. *Polym. J.* **1972**, *3*, 600.
(6) Doll, W. W.; Lando, J. B. *J. Macromol. Sci. Phys. B* **1970**, *4*, 309.
(7) Bachman, M. A.; Lando, J. B. *Macromolecules* **1981**, *14*, 40.
(8) Gal'perkin, Y. L.; Strogalin, Y. V.; Mlenik, M. P. *Vysokomol. Soed.* **1965**, *7*, 933.
(9) Glass, A. M.; McFee, J. H.; Bergman, J. G., Jr. *J. Appl. Phys.* **1971**, *42*, 5219.
(10) McFee, J. H.; Bergman, J. G., Jr.; Cram, G. R. *Ferroelectrics* **1972**, *3*, 305.

(11) Nakamura, K.; Wada, Y. *J. Polym. Sci., Part A-2* **1971**, *9*, 161.
(12) Matsushige, K.; Nagata, K.; Imada, S.; Takemura, T. *Polymer* **1980**, *21* (12), 1391.
(13) Carbeck, J. D.; Rutledge, G. C. *Macromolecules* **1996**, *29*, 5190.
(14) Glatter, O.; Kratky, O. *Small-Angle X-ray Scattering*; Academic Press: London, 1982.
(15) BaltaCalleja, F. J.; Vonk, C. G. *X-ray Scattering of Synthetic Polymers*; Elsevier: Amsterdam, 1989.
(16) Murthy, N. S.; Bednarcayk, C.; Moore, R. A. F.; Grubb, D. T. *J. Appl. Polym. Sci., Part B: Polym. Phys.* **1996**, *34*, 821.
(17) Grubb, D. T.; Prasad, K. *Macromolecules* **1992**, *25*, 4575.
(18) Grubb, D. T.; Prasad, K.; Adams, W. W. *Polymer* **1990**, *32*, 1167.
(19) Crist, B., Jr. *J. Appl. Crystallogr.* **1979**, *12*, 27.
(20) Matyi, R. J.; Crist, B., Jr. *J. Polym. Sci., Part B: Polym. Phys.* **1978**, *16*, 1329.
(21) Perret, R.; Ruland, W. *J. Appl. Crystallogr.* **1969**, *2*, 209.
(22) Perret, R.; Ruland, W. *J. Appl. Crystallogr.* **1970**, *3*, 525.
(23) Ruland, W.; Dewaelheyns, A. *J. Sci. Instrum.* **1967**, *44* (3), 236.
(24) Strobl, G. R.; Schneider, M. *J. Polym. Sci., Part B: Polym. Phys.* **1980**, *18*, 1343.
(25) Marquardt, D. W. *J. Soc. Ind. Appl. Math.* **1963**, *11*, 431.
(26) Keller, A. J. *J. Polym. Sci.* **1955**, *15*, 31.
(27) Schultz, J. M. *Polymer Materials Science*; Prentice-Hall: Englewood Cliffs, NJ, 1974; p 126.
(28) Hosemann, R. *Z. Phys.* **1950**, *128*, 1, 465.
(29) Hosemann, R.; Bagchi, S. N. *Direct Analysis of Diffraction by Matter*; North-Holland: Amsterdam, 1962; p 302.
(30) Bonart, R.; Hosemann, R. *Kolloid Z. Z. Polym.* **1962**, *186*, 16.
(31) Guinier, A.; Fournet, G. *Small Angle Scattering of X-Rays;* Wiley: New York, 1955.
(32) Schultz, J. M.; Lin, J. S.; Hendricks, R. W.; Lagasses, R. R.; Kepler, R. G. *J. Appl. Phys.* **1980**, *51*, 5508.
(33) Welch, G. J.; Miller, R. L. *J. Polym. Sci., Polym. Phys. Ed.* **1976**, *14*, 1683.
(34) Clark, E. S.; Muus, L. T. *Z. Kristallogr.* **1962**, *117*, 119.
(35) Clark, E. S.; Muus, L. T. *Z. Kristallogr.* **1962**, *117*, 108.
(36) Wunderlich, B.; Grebowicz, J. *Adv. Polym. Sci.* **1984**, *60/61*, 1.

MA990896W